inorganics

MDPI

Article

Printed High-Performance Visible-Light Photodetectors Using $CsPbBr_3$ Perovskite Quantum Dots and Integrated Lithography

Amal M. Al-Amri [1,*], Ghadah Al-Harbi [2], Roaa Sait [2], Nazek El Atab [3], Camelia Florica [4] and Ahad Syed [4]

[1] Department of Physics, College of Science and Arts, King Abdulaziz University, Rabigh 21911, Saudi Arabia
[2] Department of Physics, King Abdulaziz University, Jeddah 21589, Saudi Arabia
[3] Electrical and Computer Engineering Program (ECE), King Abdullah University of Science and Technology (KAUST), Thuwal 23955-6900, Saudi Arabia
[4] Core Laboratories, King Abdullah University of Science and Technology (KAUST), Thuwal 23955-6900, Saudi Arabia
* Correspondence: amsalamri@kau.edu.sa

Abstract

This study introduces a novel fabrication strategy that combines photolithography with printed electronics to develop high-performance photodetectors (PDs) operating in the visible spectrum. $CsPbBr_3$ perovskite quantum dot (QD)-based PDs with varying layer configurations were fabricated and characterized under 405 nm laser illumination at various intensities. The QDs were deposited onto pre-patterned, Au-coated substrates using a piezoelectric inkjet printer under ambient conditions. Under zero-bias operation, the optimized bilayer (2L) device exhibited an ultra-low dark current of 1.10×10^{-11} A, an elevated light current of 1.20×10^{-10} A, and an absolute photocurrent of 1.09×10^{-10} A. This configuration demonstrated excellent performance metrics, including a strong ON/OFF current ratio of 10.91, a calculated responsivity of 1.36×10^{-9} A/W, and a shot-noise-limited specific detectivity of 6.07×10^{5} Jones. Furthermore, the device showed stable, self-powered operation under visible light, confirming its energy-efficient sensing capabilities. This work highlights the immense potential of hybrid lithographic and printing techniques for producing low-cost, scalable, and flexible perovskite-based photodetectors, providing a promising framework for next-generation optoelectronic systems, including wearable and environmental sensing technologies.

Keywords: photodetector; perovskite quantum dot; lithography; printing technologies; sensors

Check for updates

Academic Editor: Rihui Yao

Received: 10 September 2026
Revised: 11 October 2026
Accepted: 12 October 2026
Published: 14 October 2026

Copyright: © 2026 by the authors. Licensee MDPI, Basel, Switzerland. This article is an open access article distributed under the terms and conditions of the Creative Commons Attribution (CC BY) license.

1. Introduction

Photodetectors (PDs) are optoelectronic devices that absorb light and convert optical signals to electrical signals. They represent a fundamental class of semiconductor devices with wide-ranging applications, including optical image sensors, environmental monitoring, electrocommunication, and remote sensing technologies. However, many conventional photodetectors have limited real-life applicability due to their dependence on external drivers and/or external power supplies, which are necessary to facilitate the transport of the photogenerated carriers and generate a measurable photocurrent [1,2]. To overcome these limitations, a new class of self-powered PDs has emerged, enabling photodetection without the need for an external power supply or an applied voltage [3,4]. The performance of these self-powered devices is primarily influenced by two key factors: the choice of semiconductor material used as the active layer and the efficiency of charge carrier

generation and transport under illumination [5,6]. A wide variety of materials have been explored as active layers in PDs to achieve superior optical performance. These include carbon nanotubes, graphene, transition metal dichalcogenides (TMDCs), black phosphorus, quantum dots (QDs), and organic semiconductors [7]. Among these, halide perovskite materials have garnered significant attention due to their facile synthesis, excellent light absorption, and efficient charge conversion capabilities, making them attractive candidates for high-performance optoelectronic applications [8]. All-inorganic halide perovskite ($CsPbX_3$, X = Cl, Br, I) QDs have enabled the development of transparent and flexible electronic devices [9]. For example, Wang et al. demonstrated improved performance in $CsPbBr_3$ QD-based PD by embedding the QDs in a P3HT matrix and applying ligand modifications. This approach led to a nearly 10-fold increase in response speed compared to devices utilizing unmodified QDs [10]. In 2016, Song et al. introduced a conformable PD fabricated via a straightforward solution-processing method using atomically thin (2D) nanosheets of $CsPbBr_3$. These nanosheets were assembled into high-quality, large-area films that served as flexible, ultra-thin optoelectronic layers capable of maintaining structural integrity without cracking. This approach enabled the development of mechanically robust, flexible PDs. Subsequently, Wang et al. used ZnO nanorods (NRs) as an electron transport layer (ETL) and $CsPbBr_3$ QDs as a photo-absorber to construct the perovskite PD. This configuration significantly improved the charge transport and overall device efficiency [11].

PDs can be manufactured using a variety of techniques, including, but not limited to, chemical vapor deposition (CVD), sol–gel, vapor phase transport, successive ionic layer adsorption reaction (SILAR), electrodeposition, spray pyrolysis, hydrothermal synthesis, chemical bath deposition (CBD), and modified chemical bath deposition (M-CBD) [12]. The M-CBD process enhances the conventional CBD process by introducing air bubbles into the growth solution. This is achieved by placing the CBD setup in an oven while continuously pouring the precursor solution over the substrate. The presence of air bubbles not only facilitates a more uniform deposition but also introduces oxygen into the reaction environment. As a result, M-CBD helps reduce variability in the film quality and improves the overall reliability of the deposition process [13]. Zonghui Duan et al. utilized standard photolithography and electron beam evaporation techniques to fabricate a broadband PD by incorporating copper indium diselenide (CIS) QDs into a methylammonium lead iodide ($CH_3NH_3PbI_3$) perovskite matrix. In another study, Yue Yang et al. developed a hybrid photodetector based on a $CH_3NH_3PbI_{3-x}Cl_x$ perovskite–$CsPbBr_3$ QD system using a solution-processing technique. The resulting device demonstrated a high photoresponse of 0.39 A/W and exhibited a broad spectral sensitivity spanning the 400–800 nm wavelength range [14].

Pawel E. Malinowski et al. [15] demonstrated organic photodetectors (OPDs) utilizing active layers composed of polymers and small molecules patterned through photolithography. Their study revealed that, after patterning, the devices retained their properties, achieving an external quantum efficiency (EQE) of up to 40% at a wavelength of 500 nm and exhibiting a dark current density of 1 mA/cm^2 at −2 V. In another notable work, Xiaolong Liu et al. fabricated a high-performance photodetector based on an Au/Bi_2O_2Se junction. To avoid contamination typically introduced during conventional lithographic processing, the gold electrodes were transferred using a probing tip-assisted method, ensuring a cleaner interface and improved device integrity [16]. Their results demonstrated that the PDs exhibited a broad spectral response ranging from 360 nm to 1090 nm, with a maximum photoresponsivity of 9.1 AW^{-1}. Remarkably, the devices also showed an ultrafast response time approaching 36 femtoseconds (fs). However, conventional fabrication methods such as lithography, thermal evaporation, and spin coating (commonly used in organic PDs) present several limitations. These include high production costs, significant

material waste, high energy and time consumption, and constraints in scalability, often restricting applications to small-area devices or rigid substrates.

To address the limitations of conventional fabrication techniques, printing-based methods have been developed to enhance flexibility and precision while significantly reducing manufacturing costs, making them ideal for the next generation of PDs [17]. Additive processing methods of printing technologies typically involve a single-step material deposition followed by drying, offering a streamlined and efficient fabrication route. Various printing techniques, including inkjet printing, screen printing, and spray coating, have been successfully applied in the fabrication of PDs. These methods are rapidly gaining traction due to their numerous advantages over traditional lithographic approaches, including lower production cost and compatibility with large-area and flexible substrates [18]. Numerous features of printed electronic circuits on flexible substrates have been developed in recent years by multiple researchers integrating different printing technologies. One example is a hybrid sensor fabricated using two printing techniques; screen printing was employed to deposit the sensitive resistive composite layer, while inkjet printing was used to pattern the electrodes. The high resolution enabled by inkjet printing allowed for reduced electrode spacing, thereby increasing sensitivity, especially of the capacitive component. Screen printing was chosen for the resistive layer due to the high viscosity of the toluene-sensitive composite, which was unsuitable for inkjet printing [19]. Moreover, the integration of printing techniques with solution-processing technologies is becoming increasingly prevalent in the research and development of electronic components such as transistors, diodes, and photodetectors. Owing to their low-temperature processing, reduced energy consumption, and additive nature, these methods offer a more environmentally friendly alternative to traditional semiconductor manufacturing. This shift also addresses the limitations of conventional fabrication approaches, which tend to be less adaptable and slower to evolve [20].

The hybrid approach employed in this study, combining integrated lithography with printed electronics, is designed to establish a novel fabrication strategy that leverages the precision and scalability of both techniques. This integration aims to significantly enhance device performance while optimizing manufacturing efficiency. In addition, this approach allows us to achieve the alignment accuracy typically associated with cleanroom lithography while maintaining the cost-effectiveness and scalability of printed electronics. To realize a photodetector (PD) capable of operating effectively within the visible spectrum, this work introduces a new process that merges lithographic patterning with printed electronics. The resulting device demonstrates improved sensitivity, strong photo-response in the visible range, and mechanical flexibility, highlighting the potential of this hybrid methodology for next-generation, high-performance optoelectronic systems.

2. Results and Discussion

An experimental investigation was conducted to evaluate the I-V performance of PDs fabricated using integrated lithography and printed electronics techniques. Devices incorporating one-layer (1L) and two-layer (2L) configurations of $CsPbBr_3$ QDs were examined under both dark and illuminated conditions, utilizing a 405 nm laser source with varying light intensities. Essential electrical performance parameters, such as dark current, light current, ON/OFF ratio, photocurrent, responsivity, and specific detectivity, were determined. Additionally, temporal photo-response was measured by periodically switching the light source ON and OFF to assess the device's response time to incident light. Measurements were carried out under controlled ambient conditions, and responsivity and detectivity were calculated using standard evaluation equations to assess overall photodetector performance.

2.1. I–V Characteristics

Figure 1a,b show the I–V logarithmic characteristics of a 1L and 2L PD fabricated by lithography and integrated techniques, respectively. A monochromatic light source with a wavelength of 405 nm was used to illuminate the samples. I–V measurements were conducted under both dark and illuminated conditions, with light intensities ranging from 10 mW to 80 mW. The devices were biased from +1 V to −1 V to capture performance under both forward and reverse bias conditions. As shown in Figure 1, the symmetrical shape of the I–V curves indicates a uniform distribution of the QDs across the Au electrodes and suggests the formation of effective ohmic contacts, which are critical for ensuring consistent charge transport and device performance [21,22]. The PDs exhibited very low dark current and significantly enhanced photocurrent when $CsPbBr_3$ QDs were used as the active layer. As shown in Figure 1a, the 1L device demonstrated a dark current of 2.00×10^{-12} A under zero bias, while the light current increased to 1.50×10^{-11} A under 80 mW illumination, yielding a photocurrent of 1.30×10^{-11} A. When a bias voltage of ± 1 V was applied, the dark current reached 5.00×10^{-11} A, and the light current ranged from 6.00×10^{-11} A to 1.00×10^{-10} A as the light intensity varied between 10 mW and 80 mW. Figure 1b illustrates the performance of the 2L device, which displayed a zero-bias dark current of 1.10×10^{-11} A and a light current of 1.20×10^{-10} A under 80 mW illumination, resulting in an enhanced photocurrent of 1.09×10^{-10} A. Under a ± 1 V bias, the 2L device exhibited a dark current of 4.00×10^{-10} A and a maximum light current of 5.50×10^{-10} A at 80 mW. The exceptionally low dark current is attributed to the high resistance of the perovskite grains, which effectively suppresses defect-related charge leakage. This increased resistance reduces unintended carrier injection from the perovskite layer into the electrodes in the absence of illumination, thereby improving the overall dark performance of the device [20]. Moreover, surface defects in $CsPbBr_3$ QDs may contribute to the suppression of minimal dark current by acting as trap sites that quench charge carriers in the absence of illumination. Upon light exposure, photogenerated carriers rapidly fill these defect states, enabling efficient photocurrent generation. This behavior suggests that the perovskite component of the device plays a critical role in facilitating charge separation and transport under illumination. Another important factor influencing the electrical performance of the device is the built-in electric potential, which arises from favorable energy-level alignment between the $CsPbBr_3$ QD layer and the electrode materials. This internal field enhances carrier extraction and reduces recombination, further contributing to the observed photo-response.

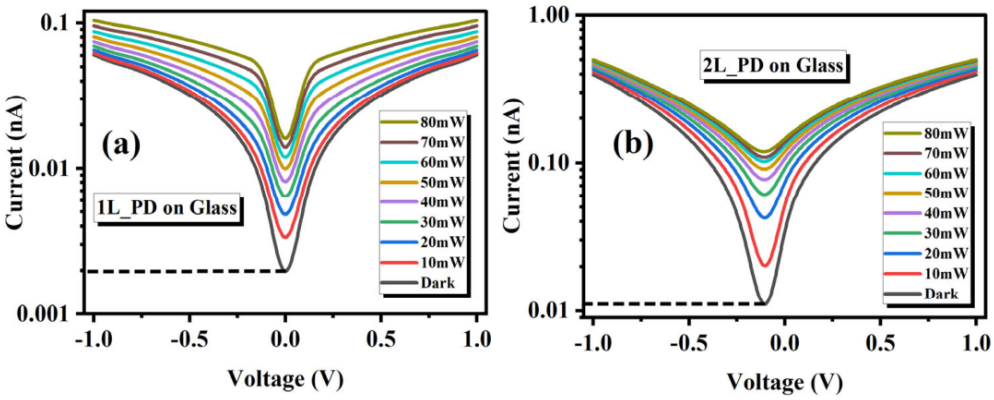


Figure 1. $CsPbBr_3$ perovskite QD photodetector: (**a**) one layer by lithography technique; (**b**) two layers by integrated lithography and printed electronics technique, under dark and different light intensities varying from 10 mW to 80 mW using a 405 nm laser as the light source.

If the built-in electric potential at the heterojunction is sufficiently strong and the energy levels are well aligned within the device structure, the $CsPbBr_3$ QDs can effectively contribute to enhanced photocurrent generation, even in the presence of relatively high layer resistance. This favorable band alignment facilitates efficient charge separation and transport across the interface. However, the precise behavior of the energy bands under practical operating conditions remains unclear, as limited information is currently available regarding their dynamic shifts and interactions in real device environments [23]. Another notable feature of the $CsPbBr_3$ QD-based PD, as indicated by the I–V curves, is the presence of a substantial photocurrent, on the order of several nanoamperes, even at zero bias. This behavior suggests that the device can operate without any external driving voltage, highlighting its potential as a self-powered PD. The self-powered operation is primarily attributed to the photovoltaic effect, whereby light-induced charge separation occurs naturally due to internal electric fields within the device, eliminating the need for an external power source to generate a detectable signal [24,25].

The I–V characteristics of the photodetectors fabricated via lithography (1L) and the integrated lithography–printing technique (2L), both under dark and illuminated conditions, are shown in Figure 1. The data clearly indicate that both dark current and photocurrent are significantly higher in the 2L device compared to the 1L counterpart, particularly under illumination. This enhanced performance in the 2L structure can be attributed to an improved ability to generate electron–hole pairs within the perovskite layer and efficiently transport them through the active material, coupled with more effective charge collection at the electrodes. Two primary mechanisms contribute to this enhancement. First, the additional $CsPbBr_3$ QD layer acts as a passivating or insulating coating that reduces interfacial recombination by spatially separating the active perovskite layer from the external Au electrode. Second, the formation of a built-in potential at the interface between the two QD layers promotes more efficient carrier transport and accelerates charge extraction, thereby improving the overall device efficiency [26,27]. Muhammad Sulaman et al. [3] demonstrated a similar strategy by introducing additional layers of P3HT and ZnO to enhance the built-in potential in hybrid PbSe:$CsPbBr_{1.5}I_{1.5}$ nanocomposite-based photodetectors. Their study revealed that these polymeric and metal oxide layers played a crucial role in modulating carrier transport within the device. Specifically, the P3HT layer functioned as both a hole-transporting and hole-blocking layer, while the ZnO layer served as an electron-transporting and electron-blocking layer. This configuration effectively elevated the energy barriers for undesired carrier injection, leading to a substantial reduction in dark current and a corresponding increase in photocurrent, thereby improving the overall photo-response and performance of the photodetector [26,28].

2.2. Performance Parameters

Accurately measuring the performance parameters of a photodetector (PD) presents significant experimental challenges due to the multitude of variables that must be carefully controlled. Both electrical and radiometric parameters need to be simultaneously monitored to ensure reliable results. In this study, we evaluated key performance metrics, including dark current, light current, ON/OFF ratio, photocurrent, specific detectivity (D*), and responsivity (R), as summarized in Table 1.

Among these, responsivity is a critical parameter for quantifying the sensitivity of the PD to incident light; it is calculated using the following equation:

$$R = \frac{I_{ph}}{PS} = \frac{I_L - I_D}{PS} \quad (1)$$

Here, I_{ph} denotes photocurrent, I_L denotes light current, I_D denotes dark current, S is the effective area of the device, and P is the intensity of incident light. Responsivity (R) is the ratio of the fundamental element of the electrical output signal of the detector to the fundamental element of the input radiation power. Generally, responsivity is the measure of the effectiveness with which light energy is converted to electrical current. On the basis of current or an electric voltage, R is given in A/W or V/W, respectively. R depends upon the following parameters: the energy bandgap of the semiconductor, temperature, and the wavelength of incoming light [29].

Table 1. Performance parameters of both samples, 1L with the lithography technique (Sample 1) and 2L with integrated lithography (Sample 2) and the printed electronics technique.

Parameters	Sample 1 (0 V)	Sample 1 (±1.0 V)	Sample 2 (0 V)	Sample 2 (±1.0 V)
Area (μm^2)	7×10^7	7×10^7	7×10^7	7×10^7
Area (cm^2)	0.7	0.7	0.7	0.7
Layer Count	1	1	2	2
I_{dark} (A)	2.00×10^{-12}	5.00×10^{-11}	1.10×10^{-11}	4.00×10^{-10}
I_{light} (A)	1.50×10^{-11}	1.00×10^{-10}	1.20×10^{-10}	5.50×10^{-10}
P (W)	0.08	0.08	0.08	0.08
I_{ph} (A)	1.30×10^{-11}	5.00×10^{-11}	1.09×10^{-10}	1.50×10^{-10}
On/Off Ratio	7.50	2.00	10.91	1.38
R (A/W)	1.63×10^{-10}	6.25×10^{-10}	1.36×10^{-9}	1.88×10^{-9}
D* (Jones)	1.70×10^5	1.31×10^5	6.07×10^5	1.39×10^5

The responsivity (R) profiles of the fabricated photodetectors were evaluated to quantify their carrier extraction efficiency under varying bias conditions. At zero bias (0 V), the 2L device exhibits a superior responsivity of 1.36×10^{-9} A/W, which represents a significant order-of-magnitude improvement over the 1L device benchmark (1.63×10^{-10} A/W). This substantial enhancement is primarily driven by the thicker bilayer architecture, which optimizes optical absorption paths and improves inter-grain connectivity within the film matrix, ultimately leading to a higher yield of photogenerated electron-hole pairs. Upon the application of an external bias voltage of ±1.0 V, the responsivity profiles scale significantly, reaching 6.25×10^{-10} A/W for the 1L device and 1.88×10^{-9} A/W for the 2L device. This positive trend occurs because the localized drift field accelerates carrier transit velocities across the collection pathways, effectively suppressing charge recombination at intermediate grain boundaries and maximizing the generated photocurrent relative to the constant incident optical power.

The 2L device, fabricated using an innovative fabrication method that consists of integrating lithography and printed electronics, exhibited approximately 8.3 times higher responsivity at zero bias compared to the 1L device. Furthermore, the 2L device demonstrated approximately 3.0 times higher responsivity under an applied bias of ±1.0 V compared to the 1L device. This significant improvement highlights the effectiveness of the hybrid fabrication strategy in enhancing device sensitivity.

It is worth noting that while the 2L configuration offers a clear performance enhancement over the 1L benchmark, the absolute responsivity values (10^{-10} to 10^{-9} A/W) remain relatively low compared to idealized bulk or single-crystal perovskite photodetectors. Several physical factors contribute to these lower values. First, the device features a planar metal–semiconductor–metal geometry that lacks internal photogating or transistor-like amplification gain mechanisms, capping the upper quantum limit. Second, because the active layer consists of printed colloidal quantum dots, charge transport is strictly governed by hopping dynamics across numerous interparticle grain boundaries and residual surface ligands. These interfaces introduce significant localized trapping centers and increase non-

radiative recombination rates [3,30]. Finally, the relatively large lateral transport channel creates a long carrier transit distance, which reduces overall extraction efficiency before the photogenerated carriers are trapped [31].

The current flowing through a device when optical radiation falls on a PD is called the photocurrent. For weak radiation signals, the photocurrent (I_{ph}) is directly proportional to the incident light power and can be expressed by the following relation:

$$I_{ph} = q\eta\Phi Ag. \quad (2)$$

where q is charge, η is quantum efficiency, Φ is radiation power, A is area, and g is photoelectric current gain [29]. In this study, the measured zero-bias photocurrent for the 1L and 2L photodetectors was 1.30×10^{-11} A and 1.09×10^{-10} A, respectively, further confirming the enhanced photo-response capability of the dual-layer structure.

Bao et al. [30] developed a p–i–n structure photodetector using thin single crystals of $CH_3NH_3PbBr_3$ and $CH_3NH_3PbI_3$ perovskite. Due to their extremely low trap densities and absence of grain boundaries, these devices achieved a remarkably low noise-equivalent power of $1-2$ fA·Hz$^{-1/2}$ and a dark current of 10^{-10}A/cm^2. However, the reliance on single-crystal growth limits the scalability of such PDs for large-scale applications. To address this, Duan [] et al. fabricated a heterostructured PD by integrating a WS_2 monolayer with $MAPbI_3$ films. This design effectively suppressed charge recombination and reduced the dark current to 10^{-11} A while achieving a high detectivity of 2×10^{12} Jones. Similarly, Shen et al. [31] incorporated a polymer into the photoactive perovskite layer, which improved surface coverage and contributed to a low dark current of 8.7×10^{-5} mA/cm^2 at -0.3 V. These approaches highlight promising strategies for minimizing dark current and enhancing performance through hybrid and composite material systems.

Figure 2 presents the photoconductive transient response of the 1L $CsPbBr_3$ perovskite quantum dot photodetector (QD PD) under 405 nm monochromatic light illumination, measured at bias voltages of 0.5 V and 1 V in an ambient environment. The incident light was modulated using an electrically controlled shutter. The device exhibited sharp and reproducible current transitions in response to light switching, demonstrating consistent ON/OFF behavior over 10 illumination cycles [32,33]. The rise time (τ_r), defined as the time for the photocurrent to increase from 10% to 90% of its maximum value, and the fall time (τ_f), representing the time required for the photocurrent to decay from 90% to 10%, were evaluated. Under 405 nm laser illumination, the measured ON/OFF response time was approximately 0.5457 s, indicating fast and stable photoconductive switching performance. Figure 3 presents the photoconductive transient response of the 2L $CsPbBr_3$ perovskite QD PD under 405 nm monochromatic light illumination, measured at bias voltages of 0.5 V and 1 V in ambient conditions. The incident light was modulated using an electrically controlled shutter.

Figure 3 illustrates the transient photo-response profiles of the 2L $CsPbBr_3$ perovskite QD PD evaluated under identical 405 nm illumination and bias conditions (0.5 V and 1 V). Similar to the baseline device, the 2L photodetector demonstrates exceptional cyclic reproducibility and operational stability over extended periods of alternating light exposure. Notably, the characteristic switching time increases to 1.275 s for the bilayer structure. This variation in temporal response is directly associated with the increased carrier transport pathways and localized trapping–detrapping phenomena within the thicker, densely packed multi-layer film. However, this subtle trade-off in response speed is well-compensated by the device's peak current output; the 2L device successfully maintains significantly higher absolute photocurrent amplitudes relative to the 1L structure across all tested operational voltages, confirming the clear performance advantages of the integrated printing approach.

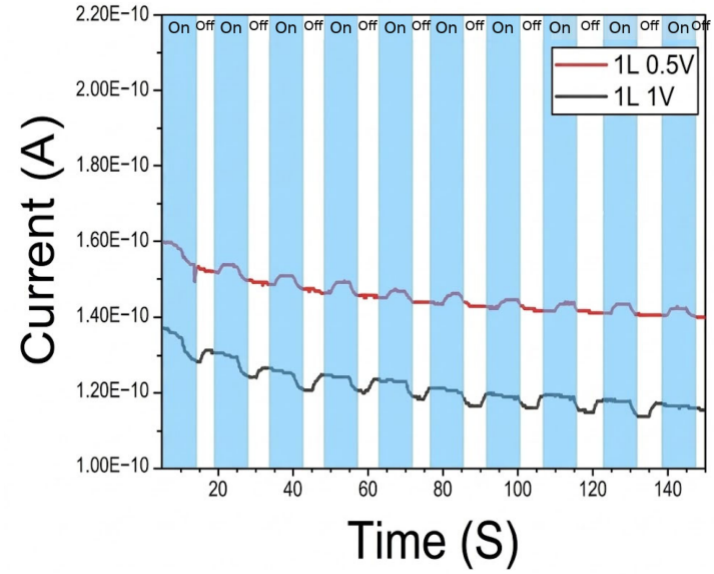


Figure 2. Time-dependent photo-response of a self-powered photodetector showing On–Off of 1L $CsPbBr_3$ perovskite QD PD at 0.5 V and 1 V bias.

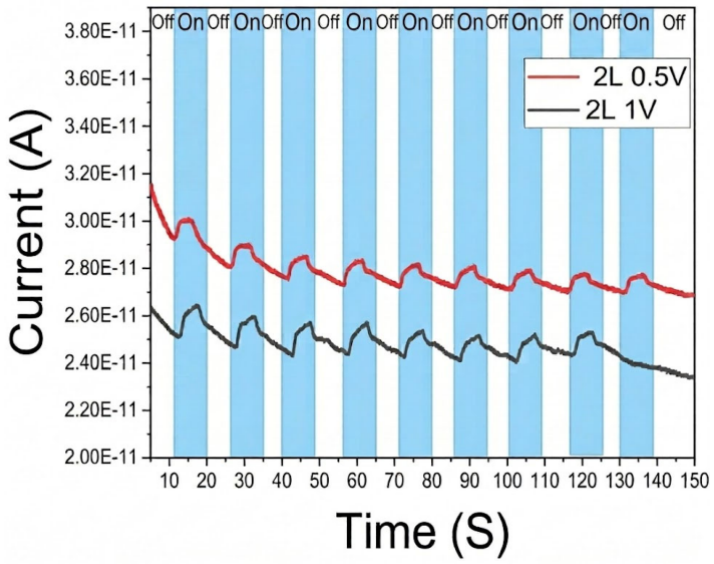


Figure 3. Time-dependent photo-response of self-powered photodetector showing On–Off of 2L $CsPbBr_3$ perovskite QD PD at 0.5 V and 1 V bias.

As summarized in Table 1, the implementation of the 2L integrated fabrication process altered the transient switching characteristics, with the characteristic response duration shifting from 0.546 s for the 1L benchmark to 1.275 s for the bilayer structure. Crucially, the 2L photodetector exhibits a significantly higher absolute photocurrent compared to its 1L counterpart. This enhancement is attributed to a stronger effective internal electric field enabled by the multi-layer architecture [3]. By stacking the printed $CsPbBr_3$ quantum dot layers, the secondary layer acts to passivate surface defects and grain boundaries, which suppresses carrier trapping. As a result, photogenerated electrons and holes are separated and extracted toward their corresponding collection electrodes more efficiently, boosting the overall steady-state current. The strategic energy-level continuity across the stacked $CsPbBr_3$ multi-layer architecture plays a critical role in directing the efficient transport of photogenerated electrons and holes. Under the influence of an applied electric field, carrier drift velocities are significantly enhanced across the well-packed quantum dot transport

channels. Consequently, even at low applied bias voltages, the field-assisted dissociation of photogenerated excitons and their subsequent transit extraction are drastically optimized. This rapid carrier sweep-out successfully outcompetes localized trapping dynamics, ultimately yielding a substantially elevated steady-state photocurrent [34].

Another important parameter used to analyze the performance of PD is detectivity (D). D is the figure of merit used to characterize the sensitivity of a photodetector and can be given as

$$D = \frac{R\sqrt{S}}{\sqrt{2qI_{dark}}} \quad (3)$$

where R is responsivity, S is the device effective area, and q is the elementary electronic charge [35]. The normalized detectivity D* (D-star) was introduced by R.C. Jones and is correlated with the unit bandwidth and detector area [36]. It is the most important detector parameter to compare detectors of the same kind with different areas. The unit of D* is $cmHz^{1/2}/W$, more popularly known as "Jones". As shown in Table 1, at zero bias (0 V), the 2L device achieves a peak specific detectivity of 6.07×10^5 Jones, outperforming the 1L device baseline of 1.70×10^5 Jones. However, a distinct performance trade-off manifests under biased operational modes. When a ± 1.0 V bias field is applied, the specific detectivity of the 2L device drops sharply to 1.39×10^5 Jones, while the 1L device decreases to 1.31×10^5 Jones. This operational degradation is directly connected to the exponential inflation of the dark current noise floor at higher bias voltages, which forces background shot-noise fluctuations upward at a rate exceeding the gains achieved in raw responsivity. Consequently, while external bias fields enhance carrier extraction velocities, the zero-bias configuration remains fundamentally critical for minimizing baseline noise floors and optimizing high-fidelity weak-signal detection. For comparison, a binary-response Se/ZnO p–n heterojunction UV photodetector exhibited a responsivity of 0.253 A/W at zero bias and 0.60 A/W at 5 V bias under 370 nm UV illumination [24]. Our findings further demonstrate the potential of scalable, cost-effective fabrication methods for perovskite-based PDs, particularly with $CsPbBr_3$ materials, utilizing integrated lithography and printed electronics techniques. Consequently, as shown in the comparative analysis of photodetector performance metrics (Table 1), the 2L device architecture, fabricated through a combination of integrated lithography and printed electronics, demonstrates a marked improvement over its 1L counterpart. While the 2L device exhibits a slightly higher baseline dark current (1.10×10^{-11} A) compared to the 1L structure (2.00×10^{-12} A), it achieves a substantially higher ON/OFF current ratio (10.91 vs. 7.50), confirming more efficient photocarrier separation and transport profiles within the bilayer framework. Notably, driven by a much higher absolute zero-bias photocurrent (1.09×10^{-10} A vs. 1.30×10^{-11} A), the 2L device exhibits superior signal-to-noise characteristics, as reflected directly in its enhanced current modulation. Furthermore, the 2L structure delivers an improved specific detectivity (6.07×10^5 Jones) and responsivity (1.36×10^{-9} A/W), both of which are critical for low-light detection and overall photodetector sensitivity. These findings highlight the potential of this hybrid fabrication approach, combining printed electronics and lithographic patterning, to produce high-performance, flexible photodetectors with enhanced sensitivity and reliable photo-response.

To resolve the apparent variance between the enhanced steady-state photocurrent in the 2L device and its prolonged transient switching times, the distinction between equilibrium transport mobility and dynamic carrier trapping must be decoupled. Under continuous 405 nm illumination (Figure 1), the stacked bilayer structure increases the absolute photo-absorber volume and fills pinhole vacancies, establishing denser macroscopic paths that lower the effective steady-state channel resistance and amplify photocarrier separation [3]. Conversely, the cyclic transient waveforms (Figures 2 and 3) capture a dynamic,

non-equilibrium environment. Stacking printed colloidal quantum dot layers introduces an abundance of structural interparticle boundary interfaces and capping ligand complexes. During alternating light-switching sequences, these defective boundary networks function as dominant carrier trapping and detrapping junctions. This high density of localized states temporarily suppresses charge sweep-out speeds, prolonging the characteristic transit duration to 1.275 s without restricting the absolute equilibrium current amplitude of the bilayer photodetector matrix.

3. Material Preparation and Device Fabrication

The perovskite QD ink used in this study was purchased from M-Quantum Solutions (Copenhagen, Denmark) and used without any chemical modification. The high-quality colloidal ink, having high stability and smooth dispersion, was used directly as a device material to maintain the inherent characteristics of an optoelectronic device. Prior to QD deposition, the substrate was thoroughly cleaned and prepared prior to the radio frequency (RF)-sputtering process to deposit a metallic electrode layer. The sputtering process was conducted using DC power at 400 W with argon (Ar) gas flowing at 25 sccm, maintaining a working process pressure of 5 mTorr. The vacuum step prior to deposition was essential for surface cleaning (plasma etching) to remove organic contaminants and improve the adhesion of the metal electrodes to the substrate. Although the substrate was subsequently transferred to atmospheric conditions for inkjet printing, this initial vacuum cleaning ensures a low-resistance ohmic contact, which is critical for efficient electron transport.

The fabrication process of the $CsPbBr_3$ QD photodetector is illustrated in Figure 4. First, the substrate was cleaned to remove surface contaminants. A shadow mask containing the desired interdigitated electrode pattern was then designed and placed directly onto the substrate. The shadow mask functioned as a stencil lithography tool, through which Au was deposited to define the electrode pattern. Unlike conventional optical photolithography, this shadow-mask-assisted stencil process does not require photoresist coating, exposure, or chemical development, thereby providing a simple physical approach for pattern definition. After Au electrode deposition, the shadow mask was removed to prepare the substrate for active layer processing.

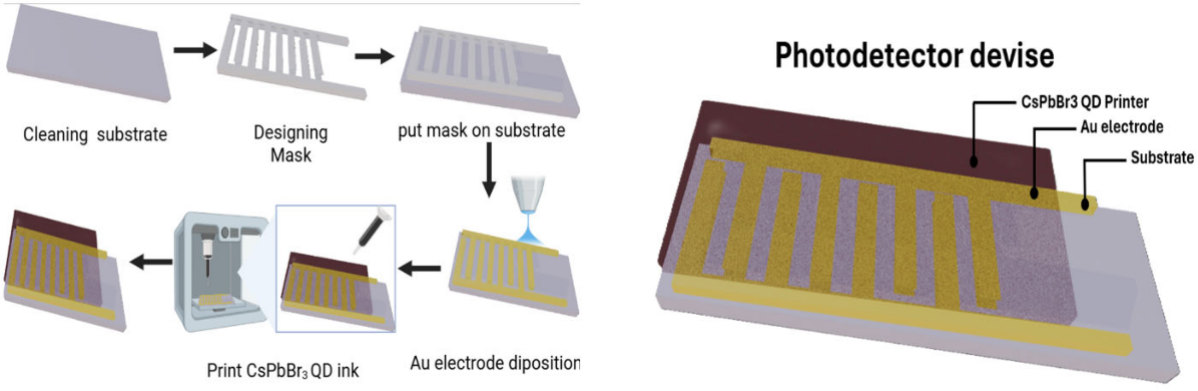


Figure 4. Fabrication process and structure schematic of the $CsPbBr_3$ QD-based PD prepared using lithography and inkjet printing methods.

To evaluate the structural influence on optoelectronic performance, two distinct device configurations were systematically prepared: a single-layer architecture (designated as 1L) and an integrated lithography–printing two-layer architecture (designated as 2L). For the 1L device, a single baseline active layer of $CsPbBr_3$ QD ink was deposited over the patterned transport channel using a piezoelectric inkjet printer under an ambient laboratory environment. Conversely, the 2L device was fabricated through an integrated technique

where a secondary, separate $CsPbBr_3$ perovskite QD functional layer was printed directly on top of the primary layer under identical ambient conditions. This non-contact, digitally driven printing technique enabled controlled and reproducible layer-wise deposition of the active and functional materials with minimal material wastage, providing uniform coverage across the active region. Following deposition, both the 1L and 2L printed films were thermally annealed on a calibrated hot plate at 100 °C for a fixed duration. This post-processing step promoted solvent evaporation, improved film adhesion, and enhanced the morphological uniformity of the QD layers, collectively optimizing the performance of the photodetectors.

4. Device Characterization

The optical response of the fabricated $CsPbBr_3$ QDs-PD was measured in a systematic way under ultraviolet (UV) light with the help of a precision Keithley source meter unit (SMU). The SMU was used to detect the current–voltage (I–V) characteristics with high sensitivity and accuracy, enabling determination of slight variations in electrical characteristics when the light intensity changes. The photo-response of the QD films was evaluated under both dark and illuminated conditions to determine key performance parameters of the photodetector, including photo-current generation, dark current contribution, and overall photoactivity. A UV light source with a fixed wavelength was used to ensure uniform exposure of all samples. All electrical measurements were conducted at room temperature under well-controlled environmental conditions to minimize external noise and ensure data accuracy and reliability. This characterization provided critical insights into the optoelectronic performance and operational stability of the perovskite QD-based PDs. As shown in Figure 5, the SEM (LEO 1530, Zeiss, Oberkochen, Germany) image confirms the uniform distribution of QDs across the substrate. The QDs exhibit varied morphologies yet maintain even surface coverage, indicating effective deposition and film quality.

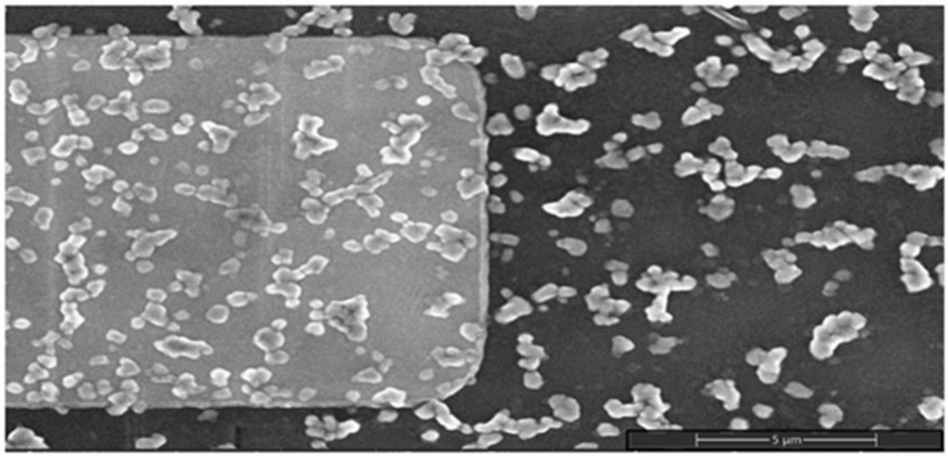


Figure 5. SEM image of the $CsPbBr_3$ QDs that uniformly cover the surface of the substrate, showing well-dispersed nanoparticles with clear morphology; scale bar = 5 µm.

5. Structural Analysis via X-Ray Diffraction (XRD)

To definitively verify the phase purity, chemical composition, and crystalline architecture of the active layers, high-resolution X-ray diffraction (XRD D8 DISCOVER A25, Bruker, Karlsruhe, Germany) characterization was performed at the KAUST Core Laboratories within the $2\theta = 10–60^\circ$ range, as illustrated in Figure 6.

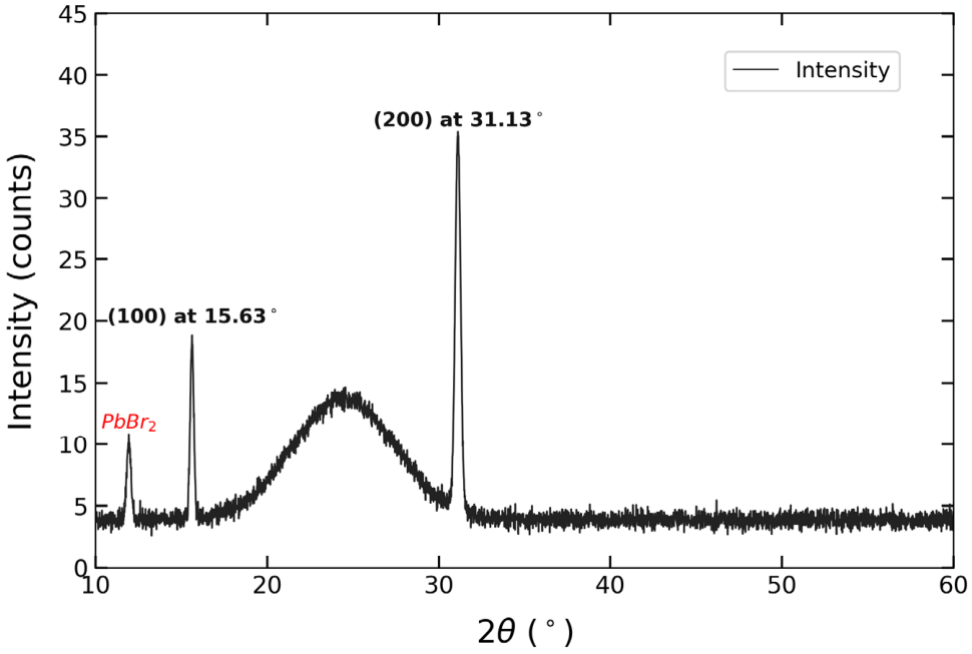


Figure 6. X-ray diffraction (XRD) pattern of $CsPbBr_3$ perovskite QD photodetector.

The diffraction spectrum reveals sharp, distinct Bragg reflections superimposed on top of a broad background envelope. This large, amorphous background halo centered between 2θ = 20° and 30° is due to the underlying glass support channel used for device fabrication. Notably, the prominent, well-defined crystalline reflection peaks appearing at precise positions of 2θ = 15.63° and 31.13° correspond precisely to the (100) and (200) diffraction planes of the standard pure cubic perovskite structure of $CsPbBr_3$, index-matched directly to JCPDS card No. 54-0752. This structural alignment is in solid agreement with recently reported configurations for $CsPbBr_3$ quantum dot arrays utilized in thin-film photodetector applications [37]. Intriguingly, the minor, lower-intensity peak resolved at 2θ = 11.95° is identified as a characteristic signature of trace unreacted lead bromide $PbBr_2$ precursors or local structural degradation into trace intermediate configurations such as $CsPb_2Br_5$ that commonly surface during low-temperature ambient drying of colloidal quantum dot inks.

According to the commercial manufacturer specifications (M-Quantum Solutions), the single-core monodisperse physical particle size of the synthesized $CsPbBr_3$ quantum dots is rated between 8.0 nm and 12.0 nm. Because the active layers were deposited via low-temperature ambient processing without subsequent high-temperature heat treatment, these physical precursor dimensions dictate the upper boundaries of the crystalline architecture within the assembled photodetector matrix, preserving the quantum-confined characteristics of the individual building blocks.

Importantly, this crystalline verification applies directly to both the 1L and 2L photodetector frameworks. Because the dual-layer (2L) device is constructed by stacking an identical secondary printed coating of the same $CsPbBr_3$ perovskite ink under standard layer-wise ambient sequences, it retains the identical high phase purity and crystalline structure of the underlying 1L baseline layer. The primary structural modification in the 2L architecture is not a phase shift but rather a denser packing density that fills up surface vacancies and passivates grain boundaries. This structural consolidation is heavily tied to the active film morphology; as shown in the cross-sectional evaluation, stacking the printed colloidal quantum dots introduces an abundance of structural interparticle boundary interfaces and capping ligand complexes. While these highly close-packed boundary networks introduce a localized density of states that slightly prolongs the transient response switching time to 1.275 s due to dynamic carrier trapping–detrapping dynamics,

they simultaneously act to passivate structural pinholes and lower macroscopic path resistance under continuous bias. Consequently, the 2L framework successfully optimizes photocarrier extraction pathways and minimizes non-radiative decay vectors, resulting in the significantly elevated steady-state photocurrent, superior signal-to-noise characteristics, and enhanced responsivity values summarized in Table 1.

6. Conclusions

In this paper, we have demonstrated a novel manufacturing strategy combining integrated photolithography with printed electronics to fabricate high-performance $CsPbBr_3$ perovskite quantum dot photodetectors. This hybrid fabrication technique successfully yielded a bilayer (2L) device structure that exhibited excellent optoelectronic characteristics under zero-bias operation, including an ultra-low dark current of 1.10×10^{-12} A, an elevated light current of 1.20×10^{-10} A, a strong ON/OFF modulation ratio of 10.91, and an enhanced responsivity of 1.36×10^{-9} A/W. Notably, the device demonstrated a stable, self-powered photo-response under visible light illumination, highlighting its potential as a viable candidate for next-generation, energy-efficient optoelectronics.

This performance enhancement is attributed to the synergistic integration of lithographic precision with the high scalability and cost-effectiveness of printed electronics. Ultimately, this approach establishes a robust pathway for fabricating low-cost, flexible, and high-sensitivity photodetector arrays. Future work will focus on the detailed passivation of material interfaces and expanding the operational spectral bandwidth, potentially unlocking broader applicability in areas such as wearable electronics, environmental monitoring, and integrated optoelectronic systems.

Author Contributions: Conceptualization, A.M.A.-A.; methodology, A.M.A.-A. and G.A.-H.; software, G.A.-H. and A.S.; formal analysis, A.M.A.-A. and G.A.-H.; investigation, A.M.A.-A., G.A.-H. and R.S.; resources, G.A.-H., R.S., C.F. and A.S.; data curation, G.A.-H.; writing—original draft preparation, A.M.A.-A.; writing—review and editing, A.M.A.-A.; visualization, G.A.-H. and A.S.; supervision, R.S. and N.E.A.; project administration, A.M.A.-A.; funding acquisition, A.M.A.-A. All authors have read and agreed to the published version of the manuscript.

Funding: This research work was supported by King Abdul-Aziz University, DSR, Jeddah, Saudi Arabia, under grant no. IPP: 477-665-2026. Therefore, the author gratefully acknowledges the technical and financial support from the Ministry of Education, King Abdul-Aziz University, DSR, Jeddah, Saudi Arabia.

Data Availability Statement: The original contributions presented in this study are included in the article. Further inquiries can be directed to the corresponding author.

Acknowledgments: The project was funded by KAU Endowment (WAQF) at King Abdulaziz University, Jeddah, Saudi Arabia. The authors therefore acknowledge the WAQF and the Deanship of Scientific Research (DSR) for technical and financial support.

Conflicts of Interest: The authors declare no conflicts of interest.

References

1. Qiu, Q.; Huang, Z. Photodetectors of 2D Materials from Ultraviolet to Terahertz Waves. *Adv. Mater.* **2021**, *33*, 2008126. [CrossRef]
2. Sarkar, K.; Hossain, M.; Devi, P.; Rao, K.D.M.; Kumar, P. Self-Powered and Broadband Photodetectors with GaN: Layered rGO Hybrid Heterojunction. *Adv. Mater.* **2019**, *6*, 1900923. [CrossRef]
3. Sulaman, M.; Yang, S.; Bukhtiar, A.; Tang, P.; Zhang, Z.; Song, Y.; Imran, A.; Jiang, Y.; Cui, Y.; Tang, L.; et al. Hybrid Bulk-Heterojunction of Colloidal Quantum Dots and Mixed-Halide Perovskite Nanocrystals for High-Performance Self-Powered Broadband Photodetectors. *Adv. Funct. Mater.* **2022**, *32*, 2201527. [CrossRef]
4. Yu, P.; Hu, K.; Chen, H.; Zheng, L.; Fang, X. Novel p–p Heterojunctions Self-Powered Broadband Photodetectors with Ultrafast Speed and High Responsivity. *Adv. Funct. Mater.* **2017**, *27*, 1703166. [CrossRef]

5. Wu, E.; Wu, D.; Jia, C.; Wang, Y.; Yuan, H.; Zeng, L.; Xu, T.; Shi, Z.; Tian, Y.; Li, X. In Situ Fabrication of 2D WS2/Si Type-II Heterojunction for Self-Powered Broadband Photodetector with Response up to Mid-Infrared. *ACS Photonics* **2019**, *2*, 6. [CrossRef]
6. Zeng, L.-H.; Chen, Q.-M.; Zhang, Z.-X.; Wu, D.; Yuan, H.; Li, Y.-Y.; Qarony, W.; Lau, S.P.; Luo, L.-B.; Tsang, Y.H. Multilayered PdSe2/Perovskite Schottky Junction for Fast, Self-Powered, Polarization-Sensitive, Broadband Photodetectors, and Image Sensor Application. *Natl. Libr. Med.* **2019**, *6*, 1901134. [CrossRef]
7. Yang, Y.; Dai, H.; Yang, F.; Zhang, Y.; Luo, D.; Zhang, X.; Wang, K.; Sun, X.W.; Yao, J. All-Perovskite Photodetector with Fast Response. *Springer Nat. Link.* **2019**, *14*, 291. [CrossRef]
8. Zhou, J.; Huang, J. Photodetectors Based on Organic–Inorganic Hybrid Lead Halide Perovskites. *Springer Nat. Link.* **2017**, *5*, 1700256. [CrossRef]
9. Wu, H.; Si, H.; Zhang, Z.; Kang, Z.; Zhou, L.; Zhang, S.; Zhang, Z.; Liao, Q.; Zhang, Y. All-inorganic perovskite quantum dot–monolayer MoS_2 mixed-dimensional van der Waals heterostructure for ultrasensitive photodetector. *Adv. Sci.* **2018**, *5*, 1801219. [CrossRef]
10. Shi, L.; Chen, K.; Zhai, A.; Li, G.; Fan, M.; Hao, Y.; Zhu, F.; Zhang, H.; Cui, Y. Status and Outlook of Metal–Inorganic Semiconductor–Metal Photodetectors. *Laser Photonics Rev.* **2020**, *15*, 2000401. [CrossRef]
11. Wang, H.; Zhang, P.; Zang, Z. High performance CsPbBr3 quantum dots photodetectors by using zinc oxide nanorods arrays as an electron-transport layer. *Appl. Phys. Lett.* **2020**, *116*, 162103. [CrossRef]
12. Ong, C.B.; Ng, L.Y.; Mohammad, A.W. A review of ZnO nanoparticles as solar photocatalysts: Synthesis, mechanisms and applications. *Renew. Sustain. Energy Rev.* **2018**, *81*, 536–551. [CrossRef]
13. Abdulrahman, A.F.; Ahmed, S.M.; Ahmed, N.M.; Almessiere, M.A. Novel process using oxygen and air bubbling in chemical bath deposition method for vertically well aligned arrays of zno nanorods. *Dig. J. Nanomater. Biostruct.* **2016**, *11*, 1073–1082.
14. Duan, Z.; Ning, J.; Chen, M.; Xiong, Y.; Yang, W.; Xiao, F.; Kershaw, S.V.; Zhao, N.; Xiao, S.; Rogach, A.L. Broad-Band Photodetectors Based on Copper Indium Diselenide Quantum Dots in a Methylammonium Lead Iodide Perovskite Matrix. *ACS Appl. Mater. Interfaces* **2020**, *12*, 35201–35210. [CrossRef]
15. Malinowski, P.E.; Georgitzikis, E.; Redondo, C.S.; Cheyns, D.; Steudel, S.; Schols, S. Organic photodetectors with active layer patterned by lithography. In Proceedings of the 2015 IEEE SENSORS, Busan, Republic of Korea, 1–4 November 2015.
16. Liu, X.; Li, R.; Hong, C.; Huang, G.; Author, D.P.; Ni, Z.; Huang, Y.; Ren, X.; Cheng, Y.; Huang, W. Highly efficient broadband photodetectors based on lithography-free Au/Bi2O2Se/Au heterostructures. *Nanoscale* **2019**, *11*, 20707–20714. [CrossRef]
17. Castro, H.F.; Sowade, E.; Rocha, J.G.; Alpuim, P.; Lanceros-Méndez, S.; Baumann, R.R. All-inkjetprinted bottom-gate thin-film transistors using UV curable dielectric for well-defined sourcedrain electrodes. *J. Electron. Mater.* **2014**, *43*, 2631–2636. [CrossRef]
18. Azzellino, G.; Grimoldi, A.; Natali, D.A.N.; Sampietro, M. Fully inkjet-printed organic photodetectors with high quantum yield. *Adv. Mater.* **2013**, *25*, 6829–6833. [CrossRef]
19. Rivadeneyra, A.; Loghin, F.C.; Falco, A. *Technological Integration in Printed Electronics*; IntechOpen: London, UK, 2017.
20. Wiklund, J.; Karakoç, A.; Palko, T.; Yiğitler, H.; Ruttik, K.; Jäntti, R.; Paltakari, J. A review on printed electronics: Fabrication methods, inks, substrates, applications, and environmental impacts. *J. Manuf. Mater. Process* **2021**, *5*, 89. [CrossRef]
21. Tong, G.; Li, H.; Li, D.; Zhu, Z.; Xu, E.; Li, G.; Yu, L.; Xu, J.; Jiang, Y. Dual-Phase CsPbBr3-CsPb2 Br5 Perovskite Thin Films via Vapor Deposition for High-Performance Rigid and Flexible Photodetectors. *Natl. Lib. Med.* **2017**, *14*, 1702523. [CrossRef]
22. Wang, H.; Zhang, X.; Ma, Y.; Wang, M.; Wang, J. A Universal Approach for Potassium-Passivated 2D Perovskites. *RRL Sol.* **2022**, *6*, 2101019. [CrossRef]
23. Aldakov, D.; Reiss, P. Safer-by-Design Fluorescent Nanocrystals: Metal Halide Perovskites Vs Semiconductor Quantum Dots. *J. Phys. Chem.* **2019**, *123*, 12527–12541. [CrossRef]
24. Hu, K.; Teng, F.; Zheng, L.; Zhang, Z.; Chen, H.; Fang, X. Binary response Se/ZnO p-n heterojunction UV photodetector with high on/off ratio and fast speed. *Laser Photonic Rev.* **2017**, *11*, 1600257. [CrossRef]
25. Wang, J.; Chang, Y.; Huang, L.; Jin, K. Designing CdS/Se heterojunction as high-performance self-powered UV-visible broadband photodetector. *APL Mater.* **2018**, *6*, 76106. [CrossRef]
26. Tan, C.S.; Hou, Y.; Saidaminov, M.I.; Proppe, A.; Huang, Y.S.; Zhao, Y.; Wei, M.; Walters, G.; Wang, Z.; Zhao, Y.; et al. Heterogeneous supersaturation in mixed perovskites. *Adv. Sci.* **2020**, *7*, 1903166. [CrossRef]
27. Liang, F.-X.; Ge, C.-W.; Zhang, T.-F.; Xie, W.-J.; Zhang, D.-Y.; Zou, Y.-F.; Zheng, K.; Luo, L.-B. Plasmonic hollow gold nanoparticles induced high-performance Bi2S3 nanoribbon photodetector. *Nanophotonics* **2017**, *6*, 494–501. [CrossRef]
28. Zhang, J.; Tolentino, J.; Smith, E.R.; Zhang, J.; Beard, M.C.; Nozik, A.J.; Law, M.; Johnson, J.C. Carrier transport in PbS and PbSe QD films measured by photoluminescence quenching. *J. Phys. Chem. C* **2014**, *118*, 16228–16235. [CrossRef]
29. Bielecki, Z.; Achtenber, K.; Mikołajczyk, M.K.J.; Wojtas, J.; Rogalsk, A. Review of photodetectors characterization method. *Electron. Telecommun. Optoelectron.* **2022**, *70*, 140534. [CrossRef]
30. Bao, C.; Chen, Z.; Fang, Y.; Wei, H.; Deng, Y.; Xiao, X.; Li, L.; Huang, J. Low-Noise and Large-Linear-Dynamic-Range Photodetectors Based on Hybrid-Perovskite Thin-Single-Crystals. *Welley Online Libr.* **2017**, *29*, 1703209. [CrossRef]

31. Shen, L.; Lin, Y.; Bao, C.; Bai, Y.; Deng, Y.; Wang, M.; Li, T.; Lu, Y.; Gruverman, A.; Li, W.; et al. Integration of perovskite and polymer photoactive layers to produce ultrafast response, ultraviolet-to-near-infrared, sensitive photodetectors. *Mater. Horiz.* **2016**, *4*, 242–248. [CrossRef]
32. Wang, F.; Mei, J.; Wang, Y.; Zhang, L.; Zhao, H.; Zhao, D. Fast Photoconductive Responses in Organometal Halide Perovskite Photodetectors. *ACS Appl. Mater. Interfaces* **2016**, *8*, 2840–2846. [CrossRef]
33. Pan, X.; Zhou, H.; Liu, R.; Wu, D.; Song, Z.; Tang, X.; Yang, X.; Wang, H. Achieving a high-performance, self-powered, broadband perovskite photodetector employing MAPbI3 microcrystal films. *J. Mater. Chem. C* **2020**, *8*, 2028–2035. [CrossRef]
34. Qasim, M.; Sulaman, M.; Bukhtiar, A.; Deng, B.; Jalal, A.; Sandali, Y.; Shah, N.H.; Li, C.; Dastgeer, G.; Bin, H. High-Performance Self-Powered Broadband Schottky Junction Photodetector Based on Graphene-Silicon van der Waals Heterostructure. *Energy Technol.* **2023**, *11*, 2300492. [CrossRef]
35. Zhang, W.; Qiu, F.; Li, Y.; Zhang, R.; Liu, H.; Li, L.; Xie, J.; Hu, W. Lattice defect engineering enables performance-enhanced MoS_2 photodetection through a paraelectric $BaTiO_3$ dielectric. *ACS Nano* **2021**, *15*, 13370–13379. [CrossRef]
36. Jones, R.C. Performance of detectors for visible and infrared radiation. *Adv. Electron.* **1953**, *5*, 27–50.
37. Cheng, Y.-C.; Lin, C.-Y.; Tseng, C.-H.; Tsai, M.-L.; Chiu, S.-K.; Shen, J.-L.; Chen, S.-L.; Chuang, C.; Tsai, D.-S. A low-cost broadband photodetector based on CsPbBr3 quantum dots/transfer-free eco-friendly graphene heterostructures for fast photoresponse. *Nanotechnology* **2025**, *36*, 315201. [CrossRef]

Disclaimer/Publisher's Note: The statements, opinions and data contained in all publications are solely those of the individual author(s) and contributor(s) and not of MDPI and/or the editor(s). MDPI and/or the editor(s) disclaim responsibility for any injury to people or property resulting from any ideas, methods, instructions or products referred to in the content.